RSC Advances

PAPER

View Article Online
View Journal | View Issue

Cite this: *RSC Adv.*, 2022, **12**, 31830

Click functionalized biocompatible gadolinium oxide core-shell nanocarriers for imaging of breast cancer cells†

Shifaa M. Siribbal, ‡[a] Shaista Ilyas, ‡[a] Alexander M. Renner, [a] Sumiya Iqbal,[a] Sergio Muñoz Vázquez,[b] Abubakar Moawia,[ef] Martin Valldor, [cd] Muhammad S. Hussain,[ef] Klaus Schomäcker[b] and Sanjay Mathur *[a]

Site-specific delivery using functionalized nanocarriers is in high demand in imaging applications of modern clinical research. To improve the imaging capabilities of conventionally used contrast agents and expand the targeting accuracy, functional gadolinium oxide based nanocarriers originated from homogeneous core shells structures (Gd_2O_3@SiO_2@Fe_3O_4) were developed using a multilayer formation approach. The synthesis and chemical configuration for the covalent binding of macrocyclic chelating agents and estrogen targeting molecules on these nanocarriers were designed by a two-step chemical synthesis method. Initially, SiO_2@Fe_3O_4 structures were prepared and encapsulated with a homogenous thin Gd_2O_3 overlayer. The exterior surface of the as-prepared carriers offered chemical binding with a breast cancer specific estrogen molecule, covalently grafted through a Click-Chemistry protocol. In the next step, to enhance the diagnostic imaging capabilities of these carriers, thiocyanate-linked chelator molecule, DOTA, was attached to the surface of estrogen bound Gd_2O_3@SiO_2@Fe_3O_4 using basic reaction conditions. The active amino groups before and after conjugation of estrogen molecules on the surface were quantified using a fluorescamine based approach. Due to the covalent binding of the macrocyclic chelator to the Gd_2O_3@SiO_2@Fe_3O_4 surface, core shell carriers showed potential radiolabeling efficiency using positron emitter radionuclide, gallium-68 (^{68}Ga). Intracellular uptake of estrogen-conjugated carriers was evaluated with MCF7 breast cancer cell lines using confocal laser scanning microscopy and fluorescent flow cytometry. In addition, *in vitro* cytotoxicity studies of functional nanocarriers as compared to bare nanoparticles showed reduced toxicity to HEK-293 cells demonstrating the role of surface attached molecules in preventing direct exposure of the Gd_2O_3 surface to the cells. The as-developed gadolinium based nanocarriers presented excellent capabilities as biocompatible target-specific imaging probes which indicates great potential in the field of dual-mode contrast agents.

Received 17th January 2022
Accepted 7th August 2022

DOI: 10.1039/d2ra00347c

rsc.li/rsc-advances

Introduction

Experimental pathways unifying imaging and therapeutic entities in a single carrier are desired for developing new theranostics probes capable of diagnosing the disease and delivering the therapeutic in a simultaneous action.[1] Additionally, by integrating multiple imaging components within one nanoparticulate platform, hybrid materials may become robust contrast agents (CA) for dual mode imaging to enhance the diagnosis accuracy.[2] In this context, nanoparticles (NPs) with surface-grafted functional ligands that can selectively link to an imaging unit as well as a drug molecule are of increasing interest.[3]

[a]*Institute of Inorganic Chemistry, University of Cologne, Greinstrasse 6, 50939 Cologne, Germany. E-mail: sanjay.mathur@uni-koeln.de; Tel: +49 221 470 5627*
[b]*Clinic and Polyclinic for Nuclear Medicine, University of Cologne, Kerpenerstrasse 62, 50937 Cologne, Germany*
[c]*Max-Planck-Institut für Chemische Physik fester Stoffe, Nöthnitzer Strasse 40, 01187 Dresden, Germany*
[d]*Centre for Materials Science and Nanotechnology, Department of Chemistry, University of Oslo, Blindern, 0315 Oslo, Norway*
[e]*Cologne Center for Genomics (CCG), University of Cologne, Faculty of Medicine and University Hospital Cologne, 50931 Cologne, Germany*
[f]*Center for Biochemistry, Medical Faculty, University of Cologne, 50931 Cologne, Germany*

† Electronic supplementary information (ESI) available: The EDX and SAED of as-prepared core shell nanocarriers, DLS graphs and table, additional SEM, TEM images and XRD measurements. In addition, the flow cytometry measurements of pure MCF7 breast cancer cells without the addition of nanocarriers, FITC conjugated Gd_2O_3@SiO_2@Fe_3O_4 are provided. See DOI: https://doi.org/10.1039/d2ra00347c

‡ Shifaa M. Siribbal and Shaista Ilyas contributed equally as primary author for this manuscript.

The next-generation positive (T_1) MRI contrast agents' gadolinium oxide (Gd_2O_3) NPs are growing as an excellent alternative to the current clinically available Gd^{3+}-chelates based CAs on account of their high spin paramagnetism, high stability in physiological milieu, lower toxicity, and better bioavailability achievable through surface conjugation of targeting units.[4–6] One of the major obstacles in using Gd-based materials for *in vivo* experiments is the known toxic effect of the Gd^{3+} ion.[7–9] Although gadolinium ions can be toxic, however, the Gd_2O_3 nanoparticles can be designed as benign materials and currently being investigated as promising materials for various MRI applications. For instance, BSA and lactobionic acid coated gadolinium-based NPs are known as nontoxic to the different cell lines at the higher concentration and for a longer period of time.[10,11] In another study, Gd_2O_3 particles showed excellent (100%) cell viability after their injection into mice up to 4 weeks.[9]

Tumor imaging *via* MRI can be upgraded by active and passive targeting and literature shows several reports on the use of gadolinium as a contrast agent in different biological assays. For example, gadolinium oxide particles covered with polymers such as polyacrylic acid or conjugating sericin enhanced magnetic resonance imaging with higher T1 relativity at tumor site in human brain glioma cells.[12,13] Also doping the gadolinium oxide particles with mesoporous silica enhanced T1 contrast of gadolinium due to silica geometrical confinement.[14–16] Recent studies have revealed that the conjugation of Gd^{3+} complexes with iron oxide NPs, and the combination of Gd_2O_3 NPs with other magnetic materials, such as Fe_3O_4 NPs into single composite particles leads to the enhancement of T1 and T2 contrast in MRI. In case of a thin gadolinium shell, nanocomposites provided higher relativity than a thick shell during MRI examinations.[18] *In vivo* and *in vitro* studies during different applications, the gadolinium labeled iron oxide nanoparticles showed brighter-effects in T1-weighted MRI and iron nanoparticles were used as spin–spin relaxation (T2).[19] To significantly enhance the T1 relaxation time without decreasing the T2 relaxation, iron-doped gadolinium nanoparticles were further studied by combining with hydrogenated silica to form a core–shell nanostructure with *in vivo* imaging with a significant improvement in T1/T2 dual mode.[20] These results evidently showed that gadolinium labeled iron-silica nanoparticles have potential as a contrast agent in magnetic resonance imaging. However, the optimal design of efficient and nontoxic Gd_2O_3 nanomaterials remains to date a stimulating approach for the development of biocompatible materials for cancer-specific imaging applications.

The surface chemistry of NPs is an important factor for their biomedical application, as colloidal NPs come into contact with the biological environment through their surfaces.[21,22] In general, one of the most critical aspects in the development of optimal nanoparticles is their colloidal stability and uncoated particles tend to aggregate in their dispersion in cell culture media exhibiting a significant toxic effect that limits their performance. Therefore, modifying the surface of NPs with organic molecules or hydrophilic polymers is crucial to improve

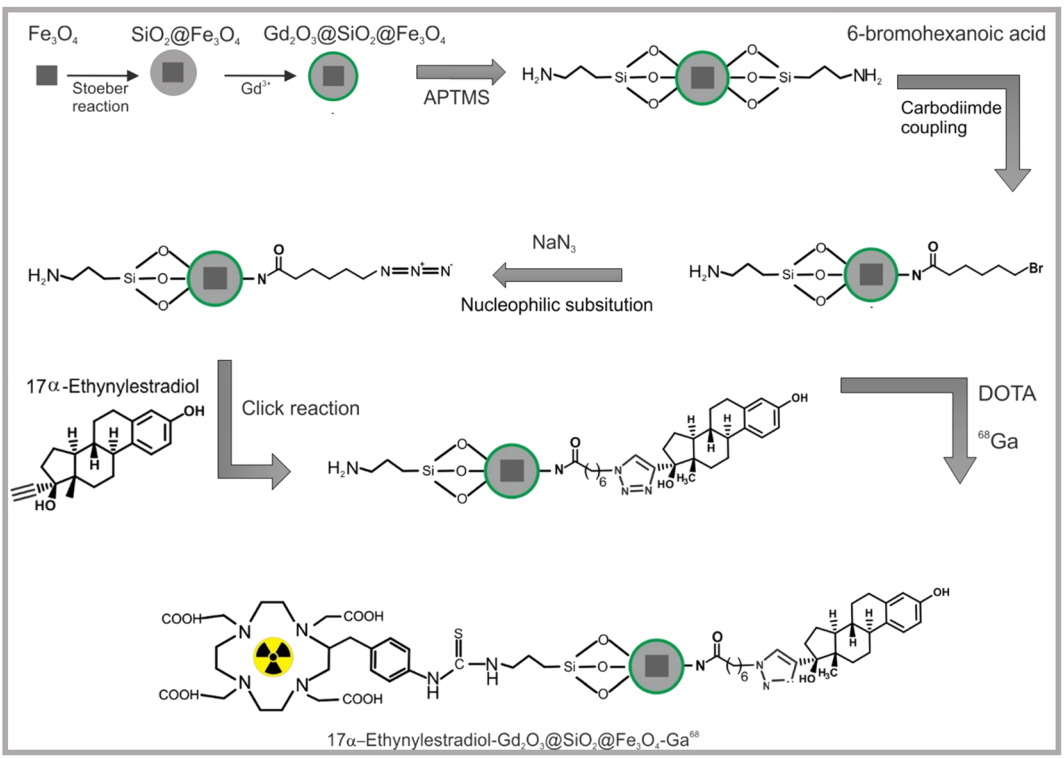

Scheme 1 Schematic illustration of the design and functionalization of Gd_2O_3@SiO_2@Fe_3O_4 (Fe_3O_4: cubes) nanocarriers with silane linker, estrogen and chelator molecules.

their stability and inherent water dispersibility.[23–28] Our study demonstrate biocompatible Gd_2O_3 based core shell nanocarriers to boost cancer cells intracellular uptake *via* ligand–receptor binding interactions. In addition, study also showed that amino silane rooted Gd_2O_3 carriers prevented the leaching of gadolinium ions which is of tremendous value to generate gadolinium based biocompatible nanomaterials for health-care application. The remaining amine residues were quantified on the surface of Gd_2O_3@SiO_2@Fe_3O_4 nanocarriers and facilitated the binding of DOTA molecules to enable imaging of the cancer cells (Scheme 1).

Results and discussion

Design and synthesis of multilayered core–shell

Homogenous structures of Gd_2O_3@SiO_2@Fe_3O_4 nanocarriers were chemically prepared based on multilayer assisted core shell approach. The formation of gadolinium oxide layer on core shell nanomaterials consists of a magnetite core, a middle SiO_2 shell as a separating layer and outer a thin Gd_2O_3 layer.[28–30] The SiO_2 shell shields the magnetic dipole interaction of Fe_3O_4 NPs to reduce the quenching effect on T1 contrast material, and consequently prevents the perturbation of the relaxation properties of T1 contrast material.[31,32]

The pathway of Gd_2O_3@SiO_2@Fe_3O_4 synthesis first includes, solvothermal method and the use of inorganic iron precursor in the presence of DMF at high temperature for the formation of nanocubes. Following, these cubes were coated with a homogeneous silica shell using controlled reaction condition *via* a Stöber reaction. The silica shell on iron oxide cubes was chemically covered with a thin layer of gadolinium oxide. The carriers were extended for click conjugation strategies: APTMs was covalently attached on the surface of nanocarriers and quantified for amino active surface. Amino-terminated Gd_2O_3@SiO_2@Fe_3O_4 carriers were linked with –Br and $–N_3$ molecules *via* nucleophilic substitution reaction. The estrogen molecules with active alkyne groups were interacted with azide modified Gd_2O_3@SiO_2@Fe_3O_4 *via* Click conjugation approach. The chelator molecules were covalently binded on estrogen-capped carriers *via* a chemical reaction using –SCN–linked DOTA compound under basic conditions.

Following, in a multistep click chemistry approach, the surface of Gd_2O_3@SiO_2@Fe_3O_4 nanocarriers was evaluated for the quantification of active amino groups.

In detail, primarily, hydrophilic (PVP-capped Fe_3O_4, quasi-cubic) and hydrophobic (oleic acid-capped Fe_3O_4, spherical) iron oxide particles, which differ substantially in size, shape, and surface texture were prepared and coated with a homogeneous silica shell to ensure stability and active linker conjugation.[33] Meanwhile, in case of the oleic acid-capped iron oxide particles, the oleic acid molecules were chemically adsorbed at NPs surfaces through the co-ordination between the metal atom and the –COO groups.[34] As a result of this chemical interaction, the hydrophobic part of oleic acid heading outwards leads to the nonpolar nature of the oleic layer around NPs surface. Therefore, to confine and control the SiO_2 coating and to stimulate the diffusion of the Fe_3O_4 NPs into the aqueous phase, non-ionic surfactant and micelles were employed. Herein, we applied an alternative strategy to use Stöber method for silica coated spherical iron oxide NPs instead of micro-emulsion approach. The treatment of nanocarriers with HCl (pH range: 3–4) resulted in the protonation of the oleate ligand and consequently the release of oleic acid from the NPs surface.[35,36] Therefore, the NPs retained their hydrophilic properties due to the presence of the –OH groups on the surface. The formation of Gd_2O_3 shell onto the surface of SiO_2@Fe_3O_4 carriers was attained through homogeneous precipitation of Gd^{3+} ion by the decomposition of urea at an elevated temperature.[37] Controlled-precipitation reaction (pH > 6) offered the formation of $Gd(OH)CO_3$ which coagulated on the negatively charged silanol groups at NP-surface. It in turn inhibits the dissolution of SiO_2 layer and prevents possible agglomeration. Thermal treatment of $Gd(OH)CO_3$@SiO_2@Fe_3O_4 NPs at 800 °C led to conversion of $Gd(OH)CO_3$ to Gd_2O_3 layer offering monodispersed Gd_2O_3@SiO_2@Fe_3O_4 structures. The crystallinity of all samples was investigated by powder X-ray diffraction measurements (Fig. 1). For both, nanocubes and nanospheres, all diffraction peaks are consistent with the standard pattern of pure Fe_3O_4 which crystallized in an inverse spinel cubic space group. The broadening of the peaks in the case of nanospheres indicates the small size of the NPs, which is confirmed by TEM analysis. XRD pattern of SiO_2@Fe_3O_4 NPs

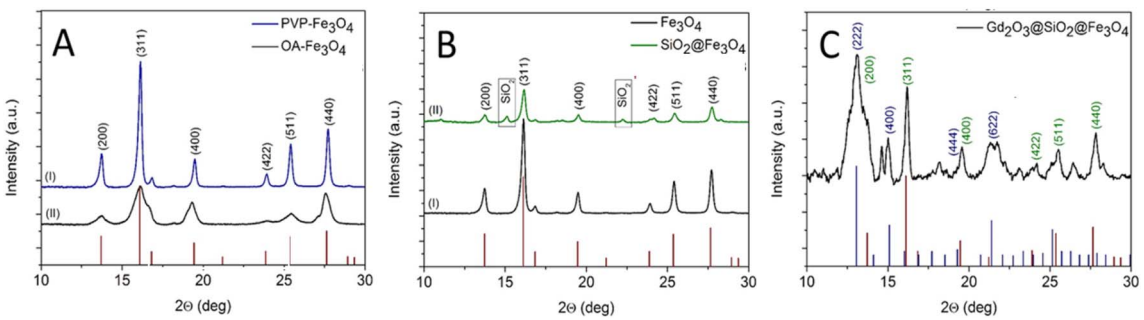

Fig. 1 X-ray diffraction patterns of: (A) iron oxide cubes and spheres, (I) PVP-capped Fe_3O_4 nanocubes, and (II) OA-capped Fe_3O_4 nanospheres, (B) Fe_3O_4 nanocubes (I) before and (II) after coating with SiO_2 layer, and (C) the as-prepared core–shell Gd_2O_3@SiO_2@Fe_3O_4 (Fe_3O_4 cubes as core) after calcination at 800 °C for 2 h.

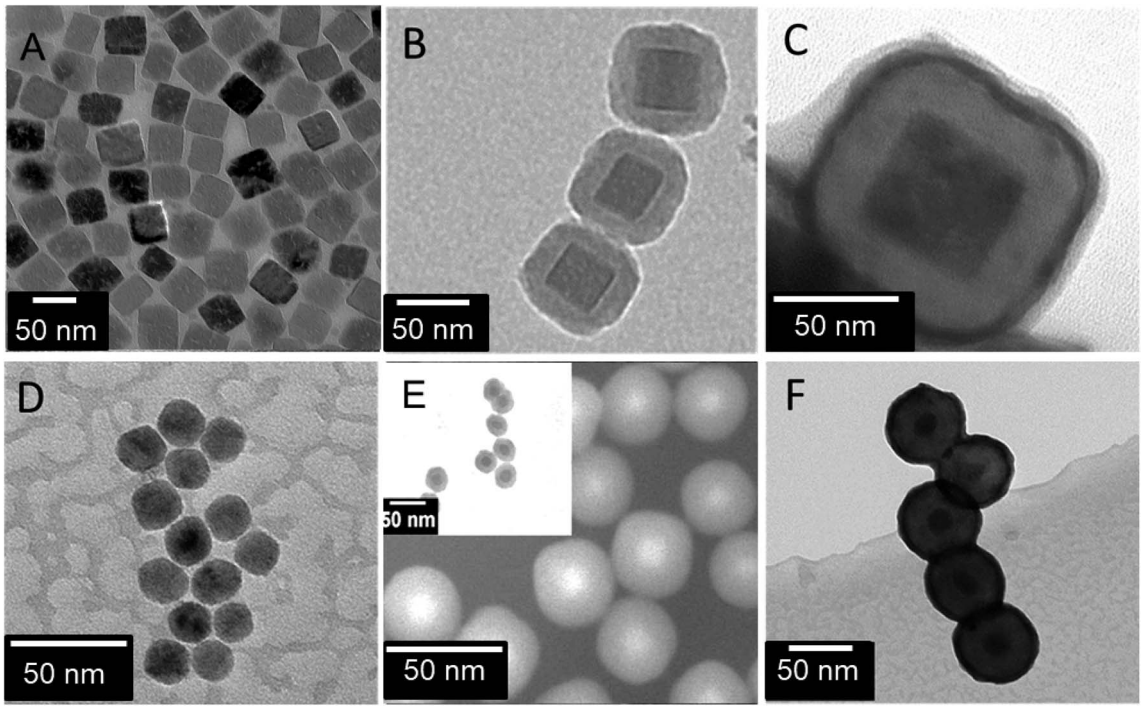

Fig. 2 Microscopic images: (A) PVP-capped-Fe_3O_4 nanocubes, (B) SiO_2@Fe_3O_4(cubes), (C) Gd_2O_3@SiO_2@Fe_3O_4(cubes), (D) OA-Fe_3O_4 nanospheres, (E) SiO_2@Fe_3O_4(spheres), and (F) Gd_2O_3@SiO_2@Fe_3O_4(spheres).

exhibited diffraction peaks similar to that of Fe_3O_4 NPs. All peaks indexed to the cubic inverse spinel structure of Fe_3O_4 confirmed that core maintained its crystallinity after SiO_2 coating. Two additional peaks with low intensity were observed, probably due to the poorly crystalline state of SiO_2 shell.[38,39] The diffraction pattern of Gd(OH)CO_3@SiO_2@Fe_3O_4 showed key characteristic peaks of Fe_3O_4, (ICDD: C72-2303). The weak intensity of the peaks can be assigned to the formation of the additional layers on the surface of Fe_3O_4 core. No other peaks were observed indicating the amorphous nature of the Gd(OH)CO_3.[40] After annealing at 800 °C (2 h), additional peaks appeared which can be directly marked as a cubic crystalline phase of Gd_2O_3 according to ICDD: 00-012-0797. The low intensity of the signals can be attributed to the thin thickness of Gd_2O_3 layer.

The transmission electron microscopy (TEM) analysis of iron oxide revealed monodispersed nanocubes with uniform structure and an average diameter of 40 ± 4 nm (Fig. 2A). The controlled-quasi cubic geometry of the resulted nanocubes is dedicated to PVP which aids NPs to select their positions during the course of orientation attachment, and thus, formation of the regular geometry.[41] The TEM analysis of other iron oxide particles showed the presence of nanospheres in the sample with an average size of 13 ± 2 nm (Fig. 2D). These uncapped spherical Fe_3O_4 NPs did not show any agglomeration trends after the detachment of oleic acid which can be due to the presence of characteristic surface charge (Fig. S2†). It has been shown in the literature that the uncovered Fe_3O_4 NPs are agglomerated compared to the OA-covered Fe_3O_4 NPs.[42] Fig. 2B shows that SiO_2@$Fe_3O_{4(cubes)}$ acquired a typical core shell structure with dark (Fe_3O_4 core) and light contrast (SiO_2 shell thickness of 20 ± 2 nm). Similar trends of homogeneous shell development (30 ± 10 nm) were observed for SiO_2@$Fe_3O_{4(spheres)}$ structures originated from spherical iron oxide (Fig. 2E). After, Gd_2O_3 coating, both, SiO_2@$Fe_3O_{4(cubes)}$ and SiO_2@$Fe_3O_{4(spheres)}$ exhibited smooth and thin Gd_2O_3 layer formation (6 ± 2 nm and 15 ± 5 nm respectively) with uniform solid core–shell structure. The images showed that the final morphology of the materials Gd_2O_3@SiO_2@$Fe_3O_{4(cubes)}$ or Gd_2O_3@SiO_2@$Fe_3O_{4(spheres)}$ obtained is influenced by the selection of the core material (Fig. 2C and F). More thickness of the Gd_2O_3 layer on SiO_2@$Fe_3O_{4(spheres)}$ as compared to SiO_2@$Fe_3O_{4(cubes)}$ may be due to the concentration of Gd^{3+} salt precursor during synthesis. Selected area electron diffraction (SAED) pattern showed polycrystalline nature of the Gd_2O_3-shell (Fig. S-3C†). The composition of the NP was further confirmed by Energy-Dispersive X-ray analysis (EDX) which displayed surface elements distribution of iron (Fe), silicon (Si), gadolinium (Gd) and oxygen (O) elements in the core shell NPs (Fig. S-3D†).[43]

FT-IR spectra demonstrated distinct peaks of α-Fe_2O_3 NPs, whereas the vibration bands at 2946, 1650, 1420, and 1276 cm^{-1} are attributed to the CH, C═O, C–N, and –CH_2, respectively, from PVP at NPs surface Fig. 3A. The strong peak at 523 cm^{-1} is ascribed to the Fe–O vibration of Fe_2O_3. The successful release of oleic acid from the surface of the NPs was confirmed by FT-IR. The spectrum of OA-Fe_3O_4 NPs showed the characteristic peaks which indicate the presence of the OA-capping ligands at the NPs surface (Fig. 3B).[44] The peaks at 2915 cm^{-1} and 2845 cm^{-1} can be related to the asymmetric and symmetric

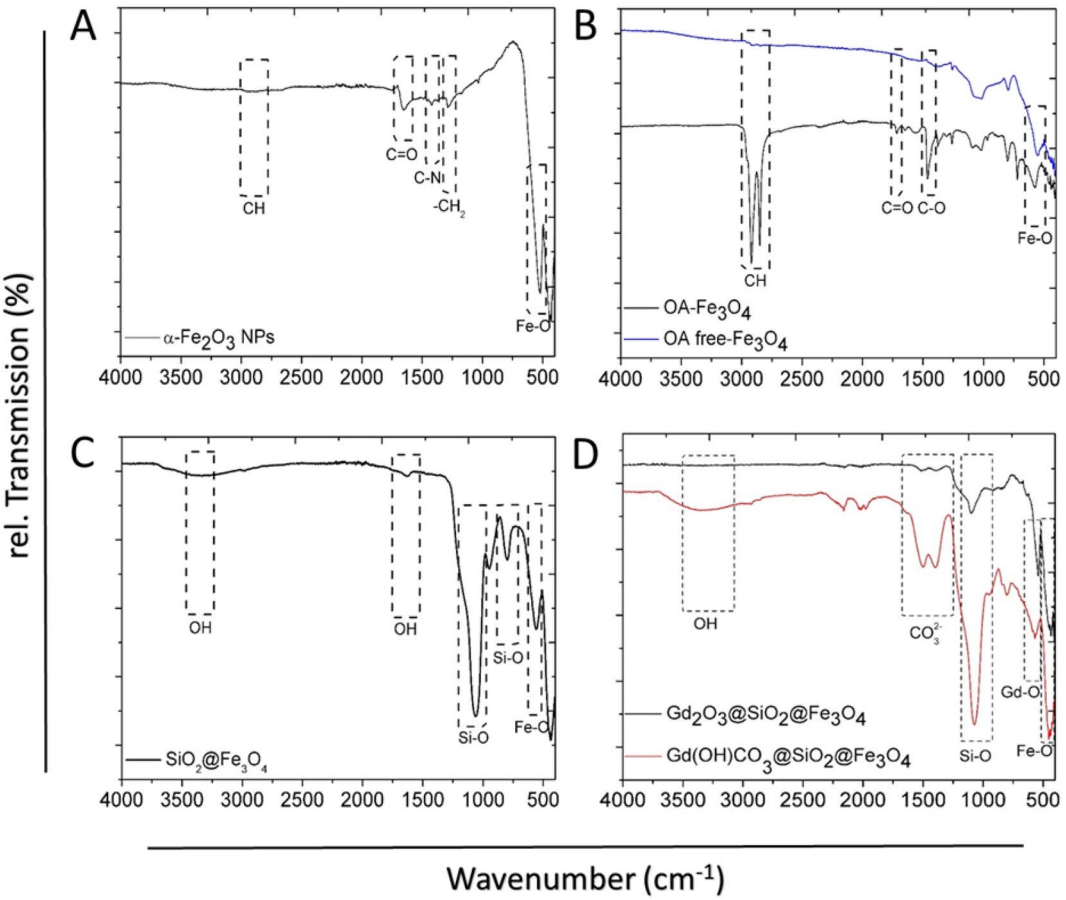

Fig. 3 FT-IR spectra of: (A) PVP-capped α-Fe_2O_3, (B) OA-capped Fe_3O_4 (black) and uncapped Fe_3O_4 (blue), (C) SiO_2@Fe_3O_4, and (D) amorphous $Gd(OH)CO_3$ shell of the precursor, and successful conversion to crystalline Gd_2O_3 layer after calcination.

stretching of $-CH_2$ groups. These peaks are absent in the OA-free NPs (Fig. 3B upper). Additionally, in contrast to the OA-NPs the peaks at 1711 cm^{-1} and 1457 cm^{-1} originate from the asymmetric and symmetric –COO stretching are not observed in the OA free NPs. The band observed around 570 cm^{-1} in both spectra is assigned to the Fe–O vibration. Surface group analysis of SiO_2@Fe_3O_4 provided further confirmation for the formation of SiO_2 shell around Fe_3O_4 NPs (Fig. 3C). The broad band at 3346 cm^{-1} corresponds to the –OH group from silanol group at NPs surface as well as the water molecules, which can be absorbed on the surface. This band is correlated with another band at 1617 cm^{-1} which is attributed to deformation vibration of the water molecules. The sharp band at 1060 cm^{-1} can be assigned to Si–O–Si asymmetric stretching vibration and the lowest intense band at 798 cm^{-1} is ascribed to Si–O–Si symmetric stretching vibration. Peak at 556 cm^{-1} is related to the Fe–O vibration. For $Gd(OH)CO_3$@SiO_2@Fe_3O_4 (Fig. 3D), a strong absorption band at 1520 cm^{-1} arises from the vibration of CO_3^{2-} group of amorphous $Gd(OH)CO_3$ shell. In addition, the broad band at 3330 cm^{-1} can be assigned to the vibrations of –OH groups. A strong band at 1093 cm^{-1} is assigned to the Si–O–Si asymmetric stretching vibration, whereas the other band at 798 cm is attributed to the Si–O–Si symmetric stretching vibration.

From the spectra of Gd_2O_3@SiO_2@Fe_3O_4, the intensity of characteristic bands of $Gd(OH)CO_3$ amorphous shell remarkably decreased after calcination (Fig. 3D). The two intense absorption bands located at 544 and 445 cm^{-1} are accounting for Gd–O stretching vibration of the Gd_2O_3 layer and Fe–O vibration of Fe_3O_4 core, respectively. The FT-IR studies provided further evidence that the amorphous $Gd(OH)CO_3$ shell can be efficiently converted to Gd_2O_3 during the calcination process, which is consistent with the results obtained from XRD and EDX.

The magnetic measurements of the SiO_2@Fe_3O_4 and Gd_2O_3@SiO_2@Fe_3O_4 carriers showed an effect on the magnetic behavior of the SiO_2@Fe_3O_4 NPs after the coating of Gd_2O_3 layer to the composite material (Fig. 4). There is a distinct separation of field-cooled (FC) and zero field-cooled (ZFC) curves, as expected for the superparamagnetic behavior of the Fe_3O_4 cores (Fig. 4B). The diversion of FC and ZFC curves starts already at 270 K, and agree with the high temperature maximum of both curves. Although the signal is relatively weak, the behavior is mimicking that of pure Fe_3O_4 NPs,[26] however, there is an additional "tail" at lower temperatures in both FC and ZFC

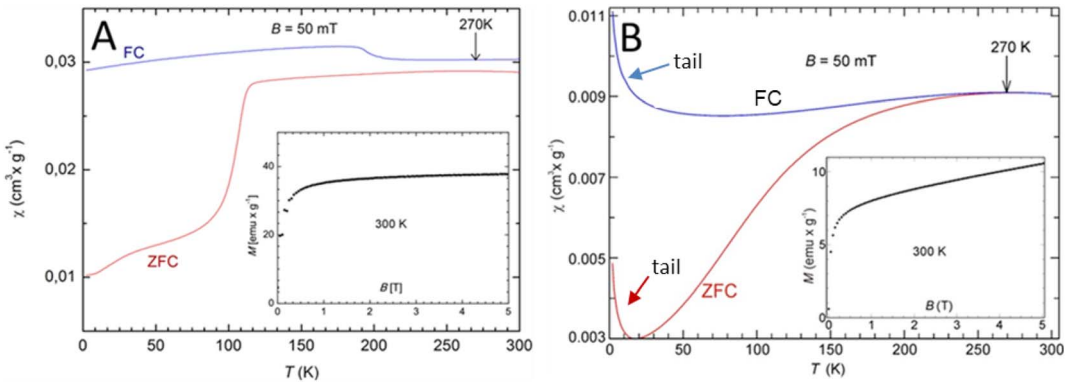

Fig. 4 Temperature dependent magnetic susceptibility (χ) of: (A) SiO_2@Fe_3O_4 and (B) Gd_2O_3@SiO_2@Fe_3O_4 and its field dependent magnetization (M) at 300 K (inset). All data are normalized to the sample mass in g. FC (field cooled) and zero field-cooled (ZFC) data are presented and they superimpose only above the marked 270 K.

curves, indicating the presence of the paramagnetic Gd-moments. Moreover, there is no clear blocking temperature, as was observed at about 120 K for the composite SiO_2@Fe_3O_4 material without the Gd_2O_3 shell (Fig. 4A).[33] The room-temperature magnetization (inset Fig. 4B) can be explained by a superparamagnetic part, which is saturated already at low fields, and a paramagnetic part, causing a linear increase with field on top of the saturation part. The absolute signal is also significantly small per gram, here ~7 as compared to about ~35 emu g^{-1} for SiO_2@Fe_3O_4, which is due to the relatively high density and, thus, the absolute weight of Gd_2O_3 relative to SiO_2@Fe_3O_4. The addition of Gd_2O_3 to the SiO_2@Fe_3O_4 composite adds a paramagnetic component across the whole measured temperature range and seems to prevent a clear magnetic blocking to occur between the Fe_3O_4 cores. Hence, the paramagnetic Gd_2O_3 shell seems to screen the core ferromagnetic moment of Fe_3O_4. This perhaps allows the magnetic NPs to act more like individual entities.

The efficiency of the surface-functionalized nanocarriers in biological systems is influenced by the physical and chemical nature of the surface-attached groups.[26,46,47] Since both carriers contain a thin gadolinium oxide layer, only the multilayer Gd_2O_3@SiO_2@Fe_3O_4 with cube-based nanocarriers were extended for chemical conjugation strategies to prove the conjugation concept. The Gd_2O_3@SiO_2@Fe_3O_4 were modified with APTMS molecules to offer free amino (–NH_2) groups. Attachment of APTMS not only provided free amino groups for further ligand conjugation, nevertheless also offered better safety to Gd_2O_3@SiO_2@Fe_3O_4 nanocarriers evident from toxicity assay. It reveals the coverage of the Gd_2O_3 surface with silane linkers, could prevent its direct exposure to the cells. FT-IR analysis demonstrated the binding of APTMS groups on Gd_2O_3@SiO_2@Fe_3O_4 surface evident in the increased intensity of Si–O–Si band at 1093 cm^{-1}, when compared to bare particles (Fig. 5A). The peaks at 1687 and 1380 cm^{-1} belonged to the –NH bending and C–N stretching vibrations, respectively, whereas the minor peak at 2933 cm^{-1} is attributed C–H vibrations. Surface modification of the as-developed carriers with estrogen molecule (17α-ethynylestradiol) was carried out *via* click chemistry approach.[48] As a first step of click-functionalization sequences, 6-bromohexanoic acid molecules were covalently binded to the surface of particles by DCC/NHS carbodiimide chemistry at 60 °C. The carboxylic groups were activated by the addition of coupling reagent dicyclohexylcarbodiimide (DCC) to create amine-reactive *O*-acylisourea ester. Following, the activated carboxylic acid were readily reacted with amino groups at the NPs surface to afford bromo groups on nanoparticles (–Br@NPs), Fig. 5B. After bromohexanoic acid attachment on particles, the FTIR spectrum showed a strong band due to C=O vibration at 1717 cm^{-1}, and the stretching vibrations of the C–H at 2965–2850 cm^{-1} indicating the successful on surface attachment of the bromo-acid (Fig. 5B). Subsequently, the bromide-terminated NPs were substituted with azide groups (–N_3) in a nucleophilic substitution SN_2 reaction with sodium azide. The absorption band at 2099 cm^{-1} corresponds to the –N_3 stretching vibrational mode verified the conjugation of 6-azido-hexanoate on the surface of particles (Fig. 5C).[49,50] The absorption band at 2990 cm^{-1} owing to the C–H vibration mode showed that the bromine precursor maintained its properties on the surface without any degradation. Successful immobilization of estrogen molecule onto the N_3@NPs surface was accomplished by an azide–alkyne cycloaddition reaction.[51] In Fig. 5D the characteristic peak of the azide vibration is completely vanished, while new absorption bands at 1624 and 1440 cm^{-1} owing to triazole ring appeared, demonstrating the completion of click reaction on NPs surface.[52] All FT-IR spectra for the modified core shell NPs demonstrated the vibration bands of the Si–O, Gd–O, and Fe–O suggesting the unchanged configuration and structure of the core shell NPs.

Moreover, the XRD pattern of estrogen-Gd_2O_3@SiO_2@Fe_3O_4 carriers that the crystallinity of the material did not change during click modification (Fig. S5†).

To evaluate the average hydrodynamic radius of bare and surface functionalized nanocarriers, dynamic light scattering measurements were conducted at pH 7.0 in water. APTMS-Gd_2O_3@SiO_2@Fe_3O_4 showed an average hydrodynamic diameter of 259 ± 11 which is larger than the diameter shown by bare Gd_2O_3@SiO_2@Fe_3O_4 indicating a change on the surface of

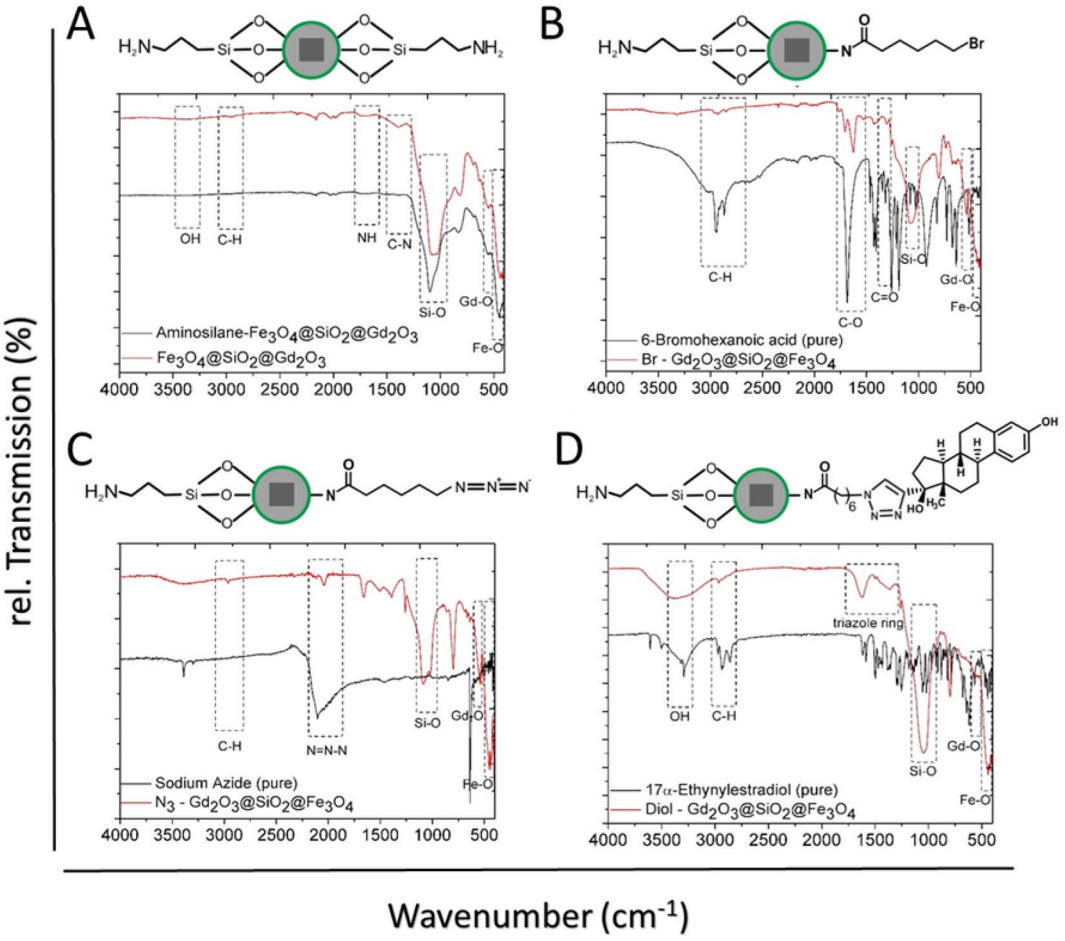

Fig. 5 The FTIR-spectra of: (A) APTMS-capped Gd_2O_3@SiO_2@Fe_3O_4 NPs, (B) attachment of the bromooctanoic acid to the surface, (C) attachment of azide groups, and (D) click chemistry between 17a-ethynylestradiol and the azide-terminated Gd_2O_3@SiO_2@Fe_3O_4 NPs.

particles after APTMS conjugation. Nanocarriers showed a further increase in hydrodynamic diameter of particles due to the binding of additional molecules including bromo and estrogen onto the surface (Table S1†). To evaluate the average surface charge of the bare and surface functionalized nanocarriers, zeta potential measurements were conducted at pH 7.0 in water. Bare Gd_2O_3@SiO_2@Fe_3O_4 exhibited a negative value of −10.1 mV due to the presence of hydroxyl groups on bare surface. After amino silane coupling, these values moved to +11.6 mV, ascribed to the positive charge from protonated amine groups in aqueous solution. After bromo and estrogen conjugation to these carriers, the surface charge showed a huge shift to −13.0 mV and −15.8 mV respectively due to the consumption of amino groups during carbodiimide coupling reaction between –NH_2 capped nanocarriers and bromo hexanoic acid (bromo: more electron density).

The thermal degradation behaviour of the bare, intermediate steps and estrogen-functionalized Gd_2O_3@SiO_2@Fe_3O_4 carriers were observed using thermogravimetric (TGA) measurements in the temperature range of 30–900 °C at a heating rate of 10 °C min^{-1} under the flow of nitrogen. TGA analysis showed that bare Gd_2O_3@SiO_2@Fe_3O_4 particles are stable up to 300 °C. At this decomposition temperature, the total mass loss is 6% which could be attributed to evaporation of the residual adsorbed solvent and water molecules on the Gd_2O_3@SiO_2@-Fe_3O_4 particles. APTMS-capped Gd_2O_3@SiO_2@Fe_3O_4 carriers showed a mass loss of in two steps. After solvent evaporation at 250 °C, the results show approximately 5% mass loss followed by second mass loss of 24% (with a total of loss of 31%), occurred in the temperature window from 250 to 900 °C which is much higher than that of bare Gd_2O_3@SiO_2@Fe_3O_4 particles. This increase in mass loss can be attributed to the thermal decomposition of the surface-grafted aminosilane (APTMS) molecules (Fig. 6B). After surface modification with 6-bromohexanoic acid, the Br-conjugated Gd_2O_3@SiO_2@Fe_3O_4 particles showed a total mass loss of 28%. At initial decomposition temperature of 300 °C, a mass loss of 6% occurred due to the removal of adsorbed solvent molecules. The other mass loss of 22% from 300 to 900 °C displayed the decomposition of bromo group related content *i.e.*, alkyl chain and amide bond (Fig. 6C). Thermal degradation of N_3-conjugated Gd_2O_3@SiO_2@Fe_3O_4 particles demonstrated a total mass loss of 18% (Fig. 6D) for the removal of azide group related content. The deviation in results as compared to Br-conjugated Gd_2O_3@SiO_2@Fe_3O_4 particles can be attributed to the different amount of NPs that present in the measured sample as well as the size distribution of NPs.

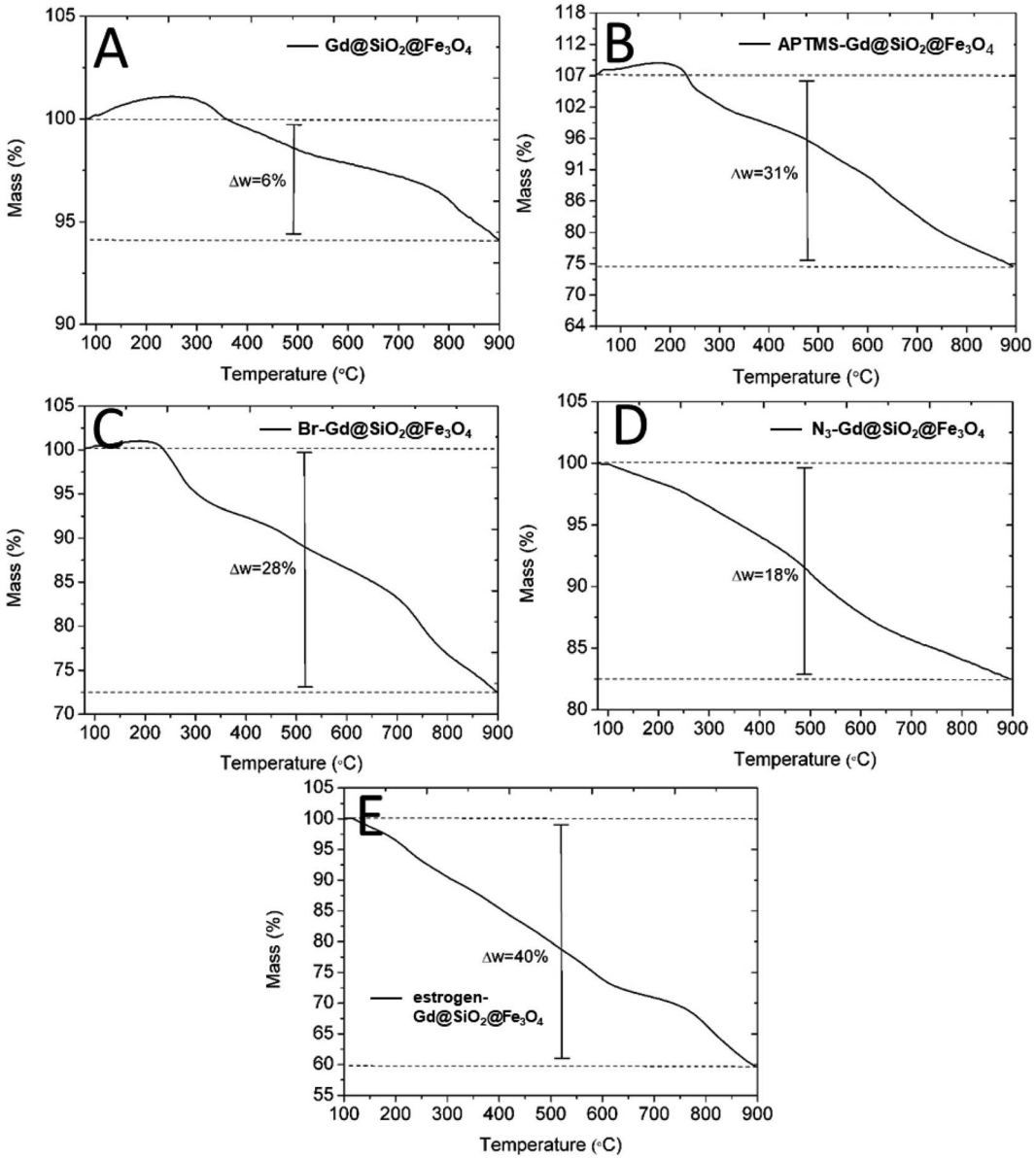

Fig. 6 Thermogravimetric analysis of the different synthetic steps of nanocarrier's functionalization: (A) bare Gd_2O_3@SiO_2@Fe_3O_4, (B) APTMS/NH_2-Gd_2O_3@SiO_2@Fe_3O_4, (C) Br–Gd_2O_3@SiO_2@Fe_3O_4, (D) N_3–Gd_2O_3@SiO_2@Fe_3O_4, and (E) estrogen-Gd_2O_3@SiO_2@Fe_3O_4. The initial increase of mass in the range from 0–300 °C in (A), (B) and (C) can be due to the minor fluctuation of the weighing balance of the machine due to the background noise.

After grafting 17α-Ethynylestradiol on Gd_2O_3@SiO_2@Fe_3O_4 surface, the larger mass loss of 40% in three steps was the consequence of the thermal decomposition of all molecules including 17α-ethynylestradiol.

Quantification of active primary amines on the surface of nanocarriers

The fluorescamine molecule based approach was chosen to quantify the active amino group on the surface of functional nanocarriers.[45a] Precisely, fluorescamine is not UV-visible active on its own but when reacts with primary amine groups it forms a product which gives an absorbance at a wavelength of 384 nm under UV-visible radiation.[45b] Moreover, the unreacted fluorescamine hydrolyzes in the presence of water and produces non UV-visible active molecules and this feature makes this approach more accurate and reliable, Scheme 2.

To calibrate this approach, the experiments were conducted with pure APTMS at its various concentrations using a constant amount of fluorescamine (stock solution: 1 mg fluorescamine/1 ml acetonitrile). The pure APTMS samples were measured by applying UV-vis spectroscopy in which the absorption of spectra generated at given wavelengths can be linked directly to the concentration of the sample, Table 1.

Based on the values, amino capped-Gd_2O_3@SiO_2@Fe_3O_4 and estrogen-coated Gd_2O_3@SiO_2@Fe_3O_4 nanocarriers were evaluated for the quantification of active surface amino ligands.

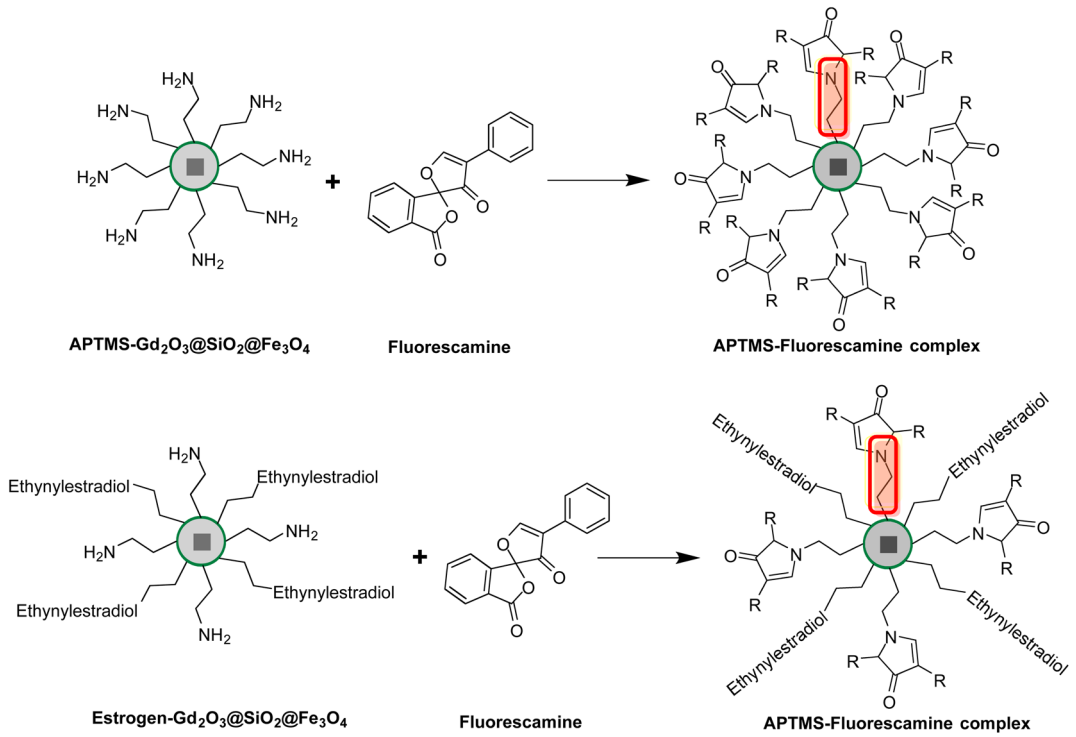

Scheme 2 The fluorescamine molecule based approach for the quantification of active amino groups on the surface of nanocarriers before and after the conjugation of estrogen molecules.

Table 1 Absorbance values of different concentration of APTMS with 50 μl of fluorescamine for calibration curve

APTMS (μl)	APTMS concentration (μg)	No of moles APTMS	Molar concentration	Absorbance (a.u.)
5.84	60	3.3×10^{-7}	3.28×10^{-7}	0.50971
25.33	260	1.4×10^{-6}	1.36×10^{-6}	1.32234
35.08	360	2.0×10^{-6}	1.9×10^{-6}	1.62892
44.83	460	2.5×10^{-6}	2.39×10^{-6}	2.20854
54.57	560	3.1×10^{-6}	2.93×10^{-6}	2.75921

Active amino groups were quantified with reference to the calibration curve using different concentration of APTMS with 50 μl of fluorescamine from the stock solution. Nanocarriers functionalized with APTMS molecules showed a peak at λ_{max} 390 nm with absorbance of 1.36 (Fig. 7C), whereas, the same amount of estrogen-capped carriers showed a peak at 390 nm with absorbance of 0.597. Table 2 (Experimental section) provides details of the quantification readout in which it can be observed that the decrease in the absorbance indicated the presence of less active amino group on the surface of estrogen capped Gd_2O_3@SiO_2@Fe_3O_4 nanocarriers compared to the APTMS functionalized nanocarrier.

Since the well-known toxic effect of Gd^{3+}-chelate compounds and Gd_2O_3-NP are inhibiting their application *in vitro* and *in vivo*, the biocompatibility of the bare Gd_2O_3@SiO_2@Fe_3O_4 and APTMS-capped Gd_2O_3@SiO_2@Fe_3O_4 was verified using as model cell-line HEK 293 (Fig. 8). Hemmer *et al.* showed that by appropriate surface functionalization, the interaction of ion leaching can be reduced which offers reduced toxicity and enhanced biocompatibility.[36] For as-synthesized bare particles showed some toxic effect to the cells (cell viability: 70%) after 48 h with 50 μg ml^{-1} NPs concentration (Fig. 8A). However, APTMS modification on these carriers offered notable cell viability. The molecules attachment on the surface of Gd_2O_3 shell, forming a protective layer on the overall core shell structure which renders its direct exposure to the cells (Fig. 8B). A minor decrease in viability of cells (78%) was observed when cells were exposed to nanocarriers with a maximum concentration of 100 μg ml^{-1}. The results are comparable to the applied concentration in reported MRI studies, declaring that the APTMS-coating on gadolinium based carrier's offers biocompatibility and decreased toxicity for cells.

Radiolabeling assessment of DOTA-conjugated estrogen-Gd_2O_3@SiO_2@Fe_3O_4 nanocarriers

To assess the imaging capabilities of as-synthesized core shell nanocarriers, we have developed an efficient radiolabeling procedure using ^{68}Ga which can be followed through radiation

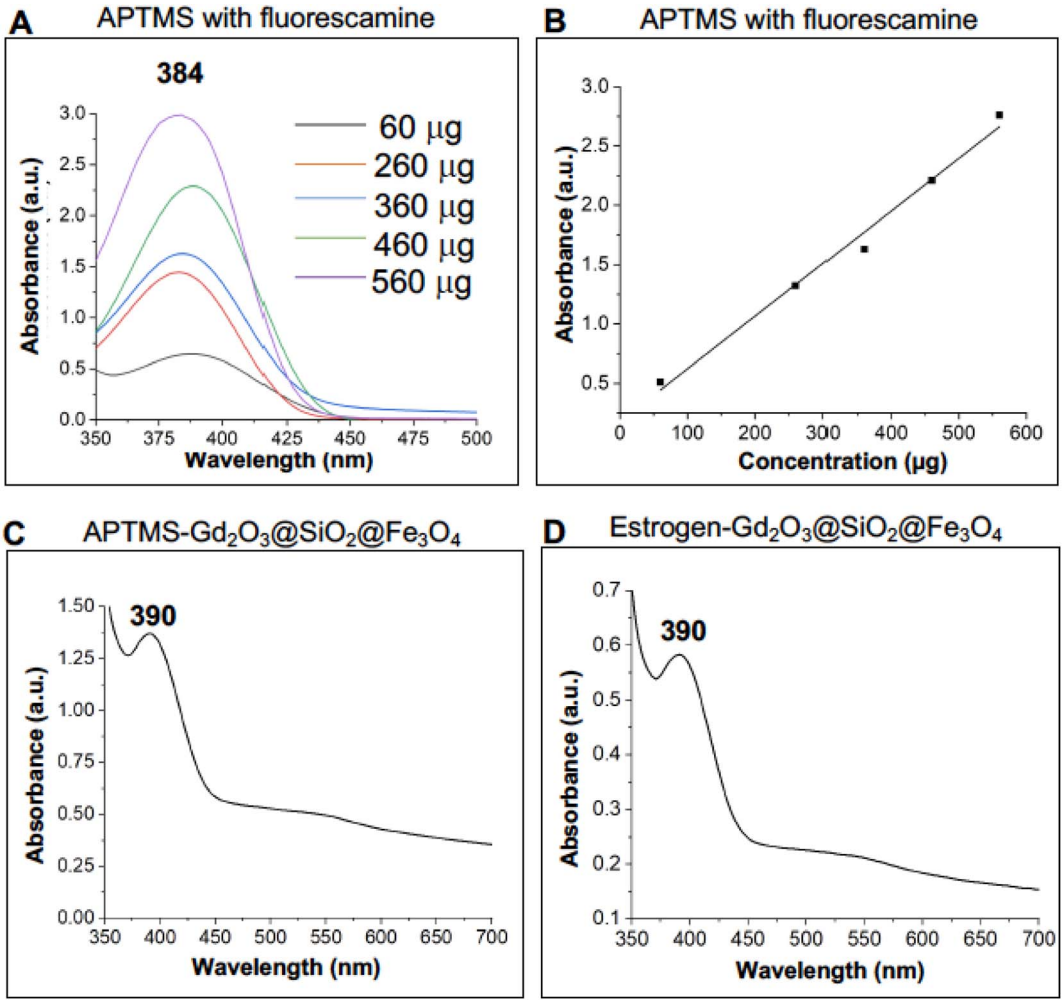

Fig. 7 Quantification of active amino groups on the surface of gadolinium based functionalized nanocarriers: (A and B) UV-visible spectra and relevant calibration curve for the quantification of pure APTMS using fluorescamine molecules. (C and D) Determination of amino groups on APTMS-Gd_2O_3@SiO_2@Fe_3O_4 and estrogen-Gd_2O_3@SiO_2@Fe_3O_4 nanocarriers.

detection as a result of radioactive decay.[53] To determine radioactive labeling yields, we used instant radio thin layer chromatography (ITLC) following APTMS-Gd_2O_3@SiO_2@Fe_3O_4 and estrogen-Gd_2O_3@SiO_2@Fe_3O_4 nanocarriers. The available amino groups at the carrier's surface provided the binding of *p*-SCN-Bn-DOTA through isothiocyanate linkage. Subsequently, radiolabeling experiments were conducted using ^{68}Ga considering its incorporation to the vicinity of DOTA chelator. As the half life time of ^{68}Ga radionuclide is 68 min, all experiments were performed for a maximum incorporation time of 60 min. Fig. 9 shows the TLC graph for the radiolabeling efficacy of ^{68}Ga-DOTA conjugated carriers. In both samples, the radiolabeling profile exhibited two different regions, the high intensity peak which correspond to the ^{68}Ga-DOTA nanocarriers, and the low intense peak for the unbound ^{68}Ga radionuclide. Radiochemical Yield (RCY) was estimated to be 80% for APTMS-

Table 2 Determination of active amino groups on the surface of nanocarriers

Nanocarriers	Absorbance (a.u.)	Concentration[a] (μg) of active amino group	No. of moles[b] of active amino group	Molar concentration[c]	No. of molecule[d] of active amino group
APTMS@SiO_2@Fe_3O_4 (2 mg)	1.36	266	1.48×10^{-6}	1.409×10^{-6}	8.9×10^{17}
Estrogen-capped Gd_2O_3@SiO_2@Fe_3O_4 (2 mg)	0.597	94	5.2×10^{-7}	4.95×10^{-7}	3×10^{17}

[a] Concentration of active amino groups on the surface of nanocarriers was calculated using slope formula. [b] No of moles = concentration (in grams)/molar mass of APTMS. [c] Molar concentration = no of moles/1.050 ml. [d] No of molecules was calculated by multiplying the no of moles with avogadro's number.

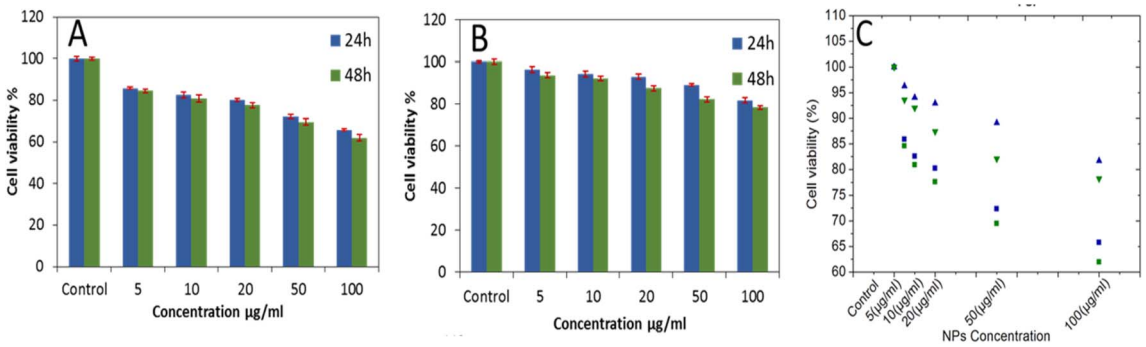

Fig. 8 *In vitro* cell viability data of cultured HEK 293 cells after incubation with: (A) bare Gd_2O_3@SiO_2@Fe_3O_4, and (B) APTMS-capped Gd_2O_3@SiO_2@Fe_3O_4, using standard MTT colorimetric assay (C) comparison of the cell viability assay: the square symbols indicate cell viabilities measured for bare Gd_2O_3@SiO_2@Fe_3O_4 and the triangle symbols for APTMS-capped Gd_2O_3@SiO_2@Fe_3O_4, viabilities after 24 and 48 h of incubation are shown in blue and green, respectively.

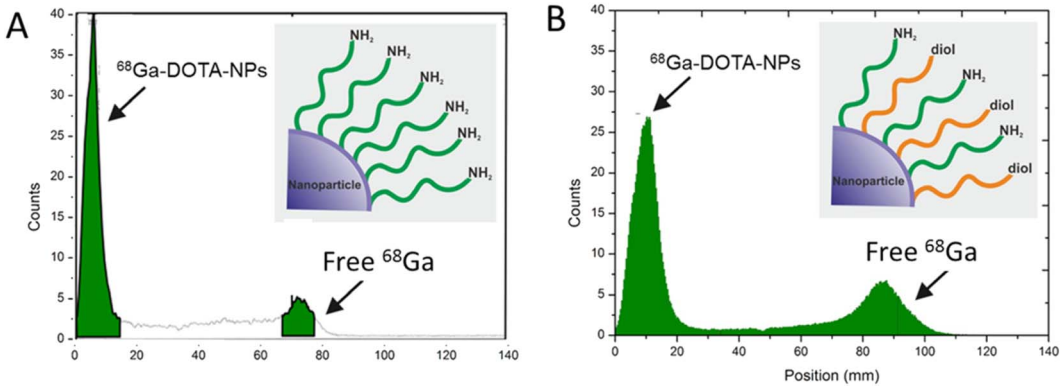

Fig. 9 TLC chromatogram of: (A) APTMS-Gd_2O_3@SiO_2@Fe_3O_4 after radiolabeling with ^{68}Ga and (B) APTMS-estrogen Gd_2O_3@SiO_2@Fe_3O_4 carriers after radiolabeling with ^{68}Ga. The radiolabeling was performed under slight acidic conditions incubating particles for 15 min at 95 °C. The radiochemical yield was determined by thin layer chromatography (ITLC). No peak was observed for free chelator molecules indicating the covalent binding of the DOTA molecule to the estrogen-capped APTMS-Gd_2O_3@SiO_2@Fe_3O_4 nanocarries.[54]

Gd_2O_3@SiO_2@Fe_3O_4 (Figure 9A) and 70% for estrogen-Gd_2O_3@SiO_2@Fe_3O_4 nanocarriers (Fig. 9B). The expected variance of radiochemical yield for both nanocarriers can be explained by the insufficient remaining –NH_2 groups on the surface of estrogen-Gd_2O_3@SiO_2@Fe_3O_4 carriers.

These amino groups are required for DOTA binding at the particle surface. Due to their consumption during carbodiimide crosslinking, the estrogen-Gd_2O_3@SiO_2@Fe_3O_4 carriers are expected to have fewer active amino groups for chelator coupling as compared to APTMS-Gd_2O_3@SiO_2@Fe_3O_4 particles. Therefore, less number of DOTA ligands might be available for ^{68}Ga incorporation, resulting in a lower radiolabeling yield. In general, DOTA ligands are specific and efficient chelating agents for Gd^{3+} ions. It has been reported that the DOTA ligand has a high affinity to coordinate with Gd^{3+}, while NODAGA (2-[1,4,7-triazacyclononan-1-yl-4,7-bis(^{t}Bu-ester)]-1,5-pentanedioic acid) ligands have a high affinity for ^{68}Ga. Moreover, gallium complex must be stable enough to avoid *trans*-chelation. Thus, a possible competition among Gd^{3+} and Ga^{3+} ions for coordinating the DOTA ligands cannot be ruled out in the solutions, which can consequently reduce the RCY. For the labeling experiment, we used a specific activity of 12.8 MBq per microgram (32 MBq per 2.5 microgram), which agrees very well with the values reported for the specific activity of PET probe.

Cellular uptake of estrogen-Gd_2O_3@SiO_2@Fe_3O_4 nanocarriers

Cell uptake of Gd_2O_3@SiO_2@Fe_3O_4 and estrogen-Gd_2O_3@SiO_2@Fe_3O_4 nanocarriers was investigated with confocal microscopy and flow cytometry measurements using MCF7 breast cancer cell-line (*in vitro*). Before their testing with cancer cells, the carriers were coupled with FITC to track their localization. Confocal imaging was performed in a time dependent manner for 1, 6 and 24 h, Fig. 10. In case of nanocarriers without ligand, it can be observed that even after 24 h only a low amount of Gd_2O_3@SiO_2@Fe_3O_4 carriers are taken up by BC cells and typically located in the intercellular area (Fig. 10 upper image). In case of estrogen-Gd_2O_3@SiO_2@Fe_3O_4 carriers, time dependent higher amount of particles is observed. After 24 h the nanocarriers accumulated in the intracellular spaces and are located next to the cell nucleus in the cytoplasm. Flow cytometry measurements were performed with Gd_2O_3@SiO_2@Fe_3O_4 and estrogen-Gd_2O_3@SiO_2@Fe_3O_4 using MCF-7 breast cancer cell

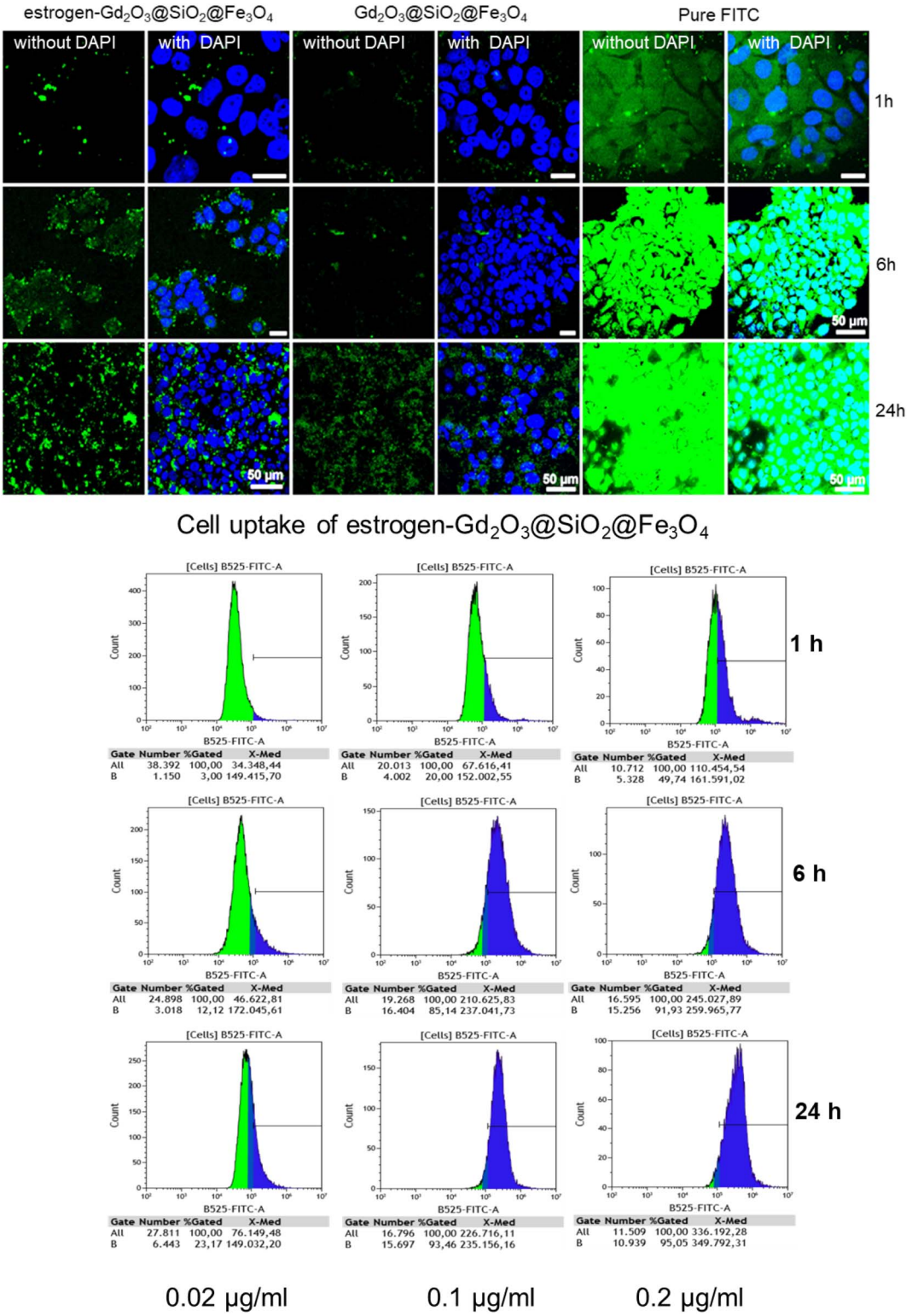

Fig. 10 Cell uptake measured by confocal microscopy (upper image) followed by flow cytometry (lower image) using Gd_2O_3@SiO_2@Fe_3O_4 and estrogen-Gd_2O_3@SiO_2@Fe_3O_4: estrogen-Gd_2O_3@SiO_2@Fe_3O_4 exhibited intracellular localization. Confocal laser scanning microscopy showed that nanocarriers has been internalized in cancer cells. MCF-7 cells were incubated with the equivalent concentration of nanocarriers for different time frames, 1 h, 6 h and 24 h. Incubation with estrogen-Gd_2O_3@SiO_2@Fe_3O_4, bare Gd_2O_3@SiO_2@Fe_3O_4 and pure FITC were evaluated. Cells were incubated (30 min) with 4′,6-diamidino-2′-phenylindole (DAPI) to give visibility to the nuclei (blue) and FITC is indicated by green fluorescence. Scale bar in each image is 50 µm. The nanocarriers were incubated with MCF7 cells lines. The cell uptake is investigated under the influence of different incubation time and nanocarriers concentration.

line. Here, Gd_2O_3@SiO_2@Fe_3O_4 and cancer cells without particles were considered as control samples, (Fig. S7†). To investigate concentration and time dependent call uptake, cancer cells were incubated with 3 different concentrations of NPs (0.1 μg ml^{-1}, 0.2 μg ml^{-1} and 0.02 μg ml^{-1}) following the investigation of cellular with 3 time periods of 1, 6 and 24 hours. Based on the negatively charged cell membrane and positively charged APTMs-capped nanocarriers, the particles stack randomly with cancer cells by electrostatically interaction leading to a cellular uptake of over 99% for all tested time periods (1 h, 6 h, and 24 h) as well as all tested concentrations. Only in case of an incubation time for 1 h and 6 h at a concentration of 0.02 μg ml^{-1}, the NPs exhibited an uptake between 74% and 85% respectively, Fig. S7.† The estrogen Gd_2O_3@SiO_2@Fe_3O_4 showed reduced cellular uptake for all tested time periods, however, in a concentration dependent manner (Fig. 10 lower image) (possibly due to its negative surface charge). For a concentration of 0.02 μg ml^{-1} during 1 h, nearly no nanoparticles were taken up or stack on cancer cell membrane, illustrating the influence of surface charge of nanoparticles. When estrogen Gd_2O_3@SiO_2@Fe_3O_4 carriers were incubated with an increased concentration of 0.1 μg ml^{-1} and 0.2 μg ml^{-1}, the probes showed increasing trends for cell uptake within the first hour of incubation. Over time, the cellular uptake increased due to the affinity of 17α-ethynylestradiol molecules to estrogen receptors indicating receptor mediated cell uptake. The slow cell uptake over a longer period of time, which can be observed in naked nanocarriers and control samples and must be taken into account, is also striking. However, an optimal ratio between randomly (non-specific) and specific cellular uptake was achieved at a concentration of 0.1 μg ml^{-1}. Under these conditions, 20% of all cells took up at least one NP within the first hour. After 6 hours, cellular uptake increased to 85% and after 24 hours to 93%. Thus, estrogen-conjugated carriers showed slower but specific cellular uptake within 24 hours compared to carriers without a targeting molecule. Remarkably, any cancer cell that took up at least one NP resulted in a positive signal.

Conclusion

Layer by layer chemical method is a versatile approach to develop new core–shell design and structure of nanocarriers such as Gd_2O_3 based SiO_2@Fe_3O_4. The as-developed carriers offer covalent attachment of more than one ligands quantitatively, on their surface, capable of individually addressing their targets in physiological environment on a single carrier system. In addition, binding the surface Gd_2O_3 thin layer with silane precursors enables biocompatibility and offer less toxicity to cells. Surface change and active ligands are decisive factors a significant increase in cellular uptake of particles, suggesting receptor-mediated endocytosis in MCF-7 cancer cell lines. The appropriate radiolabeling yield with ^{68}Ga demonstrate its potential as diagnostic nanocarriers for breast cancer research. The developed nanocarriers could be promising dual-contrast agent for T1 & T2 MRI and PET imaging expending different radionuclides.

Experimental section

Materials

Gadolinium(III) nitrate hexahydrate ($Gd(NO_3)\cdot 6H_2O$), iron(III) nitrate nonahydrate ($Fe\text{-}(NO_3)_3\cdot 9H_2O$), ammonium hydroxide solution (28–30%), tetraethylorthosilicate (TEOS), 6-bromohexanoic acid, sodium azide (NaN_3), 17α-ethynylestradiol 98%, dimethylthiazol-2-yl)-2,5-diphenyltetrazolium bromide (MTT), fluorescamine, borate buffer((0.1 mol L^{-1}), acetonitrile were all supplied by Sigma-Aldrich company. *N*,*N*-Dimethyl formamide (DMF) was obtained from Fischer Scientific and poly(*N*-vinyl-2-pyrrolidone) M_W = 55.000 (PVP) from Acros Organics. S-2-(4-Isothiocyanatobenzyl)-1,4,7,10-tetraazacyclododecane tetraacetic acid (*p*-SCN-Bn-DOTA) from macrocyclics. Phosphate-buffered saline (PBS) and Dulbecco's modified Eagle's medium (DMEM) were obtained from Gibco. The HEK 293 cells were obtained from Leibniz Institute DSMZ-German Collection of Microorganism and Cell Culture, ACC 305. The MCF-7 is human breast cancer cell line and obtained originally by pleural effusion from a female patient with metastatic disease. All reagents and solvents were used as received without further purification.

Methods

Synthesis of Fe_3O_4 nanocubes. Quasi-cubes α-Fe_2O_3 NPs were synthesized following the procedure reported by Zheng *et al.*[34] Briefly, 289 mg (0.571 mmol) $Fe(NO_3)_3\cdot 9H_2O$ were dissolved in 23 ml DMF followed by the addition of 628 mg (0.011 mmol) PVP (55 000). The mixture was transferred into a 50 ml Teflon-lined stainless autoclave and heated at 180 °C for 30 h. The obtained NPs were separated from solution by centrifugation and washed several times with water and ethanol. Afterwards NPs were dried in a vacuum oven at 60 °C for 12 h. The hematite NPs were reduced to Fe_3O_4 in an oven using forming gas (5% H_2/95% Ar) at 350 °C for 4 h with a heating rate of 10 °C min^{-1}.[33]

Synthesis of iron–oleate precursor. Iron–oleate compound, 10.8 g of iron chloride (40 mmol) and 36.5 g of sodium oleate (120 mmol) was dissolved in a mixture of 60 ml distilled water, 80 ml ethanol, and 140 ml hexane. The resulting solution was heated to 70 °C and kept for 4 h in same temperature. Afterwards, the upper organic layer containing iron–oleate complex was washed several times with 30 ml distilled water. After washing, the residual hexane was evaporated off yielding iron–oleate complex in a waxy solid form.[55]

Synthesis of Fe_3O_4 nanospheres. 18 g (20 mmol) of the synthesized iron–oleate complex and 2.8 g of oleic acid (10 mmol) were dissolved in 100 g of 1-octadecene at ambient temperature. The reaction mixture was heated to 320 °C with a heating rate of 3.3 °C min^{-1}, and kept at the same temperature for another 30 min. The reaction mixture was cooled down to ambient temperature followed by the addition of 100 ml of ethanol to precipitate the Fe_3O_4 particles. The obtained NPs were separated by centrifugation, washed with acetone and ethanol (8000 rpm for 15 mints, 6*x*) and dried overnight (16 h) at ambient temperature.[55]

Synthesis of SiO_2@Fe_3O_4 nanocarriers. 40 mg of Fe_3O_4 NPs (cubes or spheres) were dispersed in 60 ml water by sonication. 0.4 ml silicic acid solution $[SiO_x(OH)_{4-2x}]_n$ was prepared in prior by hydrolysis of 0.65 ml tetraethylorthosilicate (TEOS) in 5 ml distilled water at pH 3–4 and added to the NPs dispersion. The dispersion was stirred for 30 min, then 0.4 ml NH_4OH (28%) was added and after aging the reaction for 3 h, the particles were collected by centrifugation and redispersed in 40 ml ethanol. Afterwards, 0.08 ml of TEOS was added to the dispersion, followed by 0.65 ml of NH_4OH (28%). The reaction was stirred for 3 h at ambient temperature. Further 0.08 ml TEOS were added and the reaction mixture was kept for 12 h. The resultant SiO_2@Fe_3O_4 core shell NPs were separated by centrifugation and washed with ethanol (8000 rpm for 10 mints, 3*x*) and dried for 16 h at ambient temperature.[33]

Synthesis of Gd_2O_3@SiO_2@Fe_3O_4 nanocarriers. 1.7 ml of 0.5 M $Gd(NO_3)_3$ aqueous solution was added into a 50 ml round-bottom flask and dissolved in 10 ml of water. A 0.5067 g portion of urea was then added to the solution with stirring for 5 min to form homogeneous clear solution. Solution of well dispersed SiO_2@Fe_3O_4 (0.08345 g 10 ml^{-1}, either with cubes as core or spheres as core were added into the above solution and sonicated for 15 min). Afterwards, the flask containing the mixture was placed in an oil bath and heated at 90 °C for 6 h under vigorous stirring. The particles were separated by centrifugation and washed three times with ethanol and dried at 60 °C overnight. The particles were thermally treated at 800 °C for 2 h with a heating rate of 10 °C min^{-1} under an air atmosphere to afford Gd_2O_3@SiO_2@Fe_3O_4 both cubes and spheres based core shell structure.[18]

Synthesis of NH_2-Gd_2O_3@SiO_2@Fe_3O_4 nanocarriers. 50 ml ethanol was purged with an excess for nitrogen flow following by the addition of 30 mg Gd_2O_3@SiO_2@Fe_3O_4 nanocarriers. These carriers were sonicated for 5 min following dropwise addition of 0.5 ml APTMS under continuous supply of nitrogen. Later, the reaction was refluxed at 75 °C for 6 h.[56] The modified particles were collected *via* centrifugation at 6000 rpm and consequently washed with ethanol (3*x*) to remove any unbound aminosilane. The particles were dried at 60 °C for 16 h at ambient temperature and tested for further characterization.

Synthesis of Br–Gd_2O_3@SiO_2@Fe_3O_4 nanocarriers. 20 mg of APTMS-Gd_2O_3@SiO_2@ Fe_3O_4 NPs were dispersed in excess of toluene under nitrogen environment and dispersion was sonicated for 10 min. 14 mg of 6-bromohexanoic acid was first reacted with DCC (8 mg) followed by addition to nanoparticles dispersion under vigorous stirring. The dispersion was stirred for 20 h at 60 °C. The nanoparticles were separated by centrifugation and purified using ethanol with sonication followed by centrifugation at 4000 rpm for 10 min. The final construct was dried overnight (16 h) at ambient temperature.[24,48]

Synthesis of azide-Gd_2O_3@SiO_2@Fe_3O_4 nanocarriers. 15 mg of Br–Gd_2O_3@SiO_2@ Fe_3O_4 were dispersed in 15 ml of DMF. The nanoparticles dispersion was treated with 13 mg of sodium azide and stirred for 48 h at 60 °C. The product was isolated by centrifugation and purified with ethanol at 6000 rpm for 10 minutes (3*x*). The retrieved particles were dried overnight (16 h) at ambient temperature.[24,48]

Synthesis of estrogen-Gd_2O_3@SiO_2@Fe_3O_4 nanocarriers. Click reaction was conducted in a with azide-Gd_2O_3@SiO_2@ Fe_3O_4 NPs in mixture of ethanol and water. 50 mM 17α-ethynylestradiol was added to sodium citrate and $CuSO_4 \cdot 5H_2O$. This solution was slowly transferred to the particles dispersion and kept under stirring (500 rpm) for 48 h at 60 °C. The estrogen-modified particles were separated by centrifugation, and washed three times with water and ethanol and dried overnight (16 h) at ambient temperature.[24,48]

Quantification of active primary amines on the surface of nanocarriers

Stock solution of fluorescamine was prepared in 1 ml of acetonitrile by adding 1 mg of fluorescamine. Stock solution of APTMS was prepared by adding 500 μl of APTMS to 50 ml of borate buffer. Different concentration of APTMS stock solution in 1 ml of borate buffer (0.1 mol L^{-1}) were reacted with a 50 μl of fluorescamine stock solution (Table 1) and the absorbance of fluorescamine–amine complex was calculated with UV-visible spectrophotometry. Calibration curve at the wavelength of λ_{max} 384 nm was established using the absorbance of different concentration of APTMS with fluorescamine and the whole experiment was done in triplets (Fig. 7B). To calculate the active amino groups 2 mg of each APTMS and estrogen capped Gd_2O_3@SiO_2@Fe_3O_4 nanocarriers were dispersed in 1 ml of borate buffer and reacted with 50 μl of fluorescamine stock solution.[45a,b] The pure APTMS samples were measured by applying UV-vis spectroscopy in which the absorption of spectra generated at given wavelengths can be linked directly to the concentration of the sample, Table 2.

The UV-visible spectra of both nanocarriers was analyzed and the concentration of active amino group on the surface of nanocarriers were calculated considering slope and intercept values obtained by calibration curve [Fig. 7B and eqn (1)]

$$y = a + bx \quad (1)$$

where y = absorbance, a = intercept, b = slope and x = concentration. $y = a + bx$ where $a = 0.17843$ and $b = 0.00443$, considering calibrating in Fig. 7B.

Radiolabeling efficacy studies

Synthesis of DOTA-conjugated NPs and ^{68}Ga labeling. 1 mg of nanocarriers were suspended in 1.0 ml of 0.2 M Na_2CO_3 buffer. A stock solution of 1 mg of *p*-SCN-Bz-DOTA was dissolved in 2.5 ml 0.2 M Na_2CO_3 buffer solution under alkaline conditions. The reaction was incubated at ambient temperature for 18 h. After the incubation time the reaction was centrifuged for 10 min at 6000 rpm. The supernatant was removed and the nanocarriers were purified ultrapure water at 4000 rpm (3*x*). Later, nanocarriers were re-suspended in 950 μl of ultrapure water for labeling experiments with gallium-68. For the labeling experiments, 50 μl of the suspended NPs were mixed with 150 μl

of 2 M sodium acetate buffer in a 1.5 ml reaction vial. 200 μl of ^{68}Ga (~32 MBq) was added to the reaction vial resulting in a solution with acidic pH. The labeling mixture was incubated at 95 °C for 20 min. The radiochemical yield was determined by instant thin layer chromatography (ITLC).[57]

Cell toxicity assay. The cytotoxicity of the Gd_2O_3 nanocrystals was evaluated by means of MTT assay, using HEK 293 cells. HEK 293 cells (150 μl of 7.5 × 104 cells per ml) were cultured in a 96-well plate at 37 °C, 5% CO_2 for 24 h. The nanocrystals (1 mg NPs in 1 ml sterilized water) were incubated in the medium with different concentration, (5 μg, 10 μg, 20 μg, 50 μg, 100 μg) over a period of 24 and 48 h at 37 °C. HEK 293 cells treated only with culture media fixed as positive control. To each well, MTT (5 mg ml^{-1}) was added for 2 h incubation at 37 °C. Afterwards, the supernatant was removed, and 150 μl DMSO per well were added to resolve the formazan-crystals. The absorbance was measured at 490 nm with reference wavelength of 630 nm using Elisa reader multiplate (ELX 800, BioTek Instruments, USA).[58]

FACS measurements. MCF7 breast cancer cells were cultured in 10 ml cell medium at 37 °C, 5% CO_2 for 48 h. The cell medium was removed and the cells were washed carefully with 8 ml DPBS buffer. 4 ml trypsin was added and the cells were incubated for 5 min breaking the bonds between cells and vessel bottom. Afterwards, 5 ml cell medium including PBS was added stopping the reaction of trypsin. The cells were centrifuge at 1200 rpm for 5 min and the supernatant was discarded. The pellet was redispersed in 5 ml cell medium and transferred into a 96 well plate containing of 500 000 cells per well. Different concentrations (0.02 μg ml^{-1}, 0.1 μg ml^{-1}, 0.2 μg ml^{-1}) of nanoparticle dispersions were added to each well (except the negative control) and the well plate were incubated for 1 hour, 6 hours and 24 hours. Afterwards the cell medium was removed and the cells were washed carefully with 200 μl DPBS buffer. 100 μl trypsin was added and the 96 well plate was incubated for 3 min. To stop the reaction of trypsin, 150 μl cell medium including PBS was added and the cells were transferred into a second 96 well plate. The dispersion was centrifuged 3 times at 1200 rpm for 5 min and washed with 200 μl cell wash during each step. After the last washing step, the cells were redispersed in 100 μl cell wash and measured (CytoFLEX LX, Beckman Coulter, Germany).[24]

Instrumentation. The X-ray diffraction (XRD) analysis of nanopowders was carried out on a STOE-STADI MP diffractometer equipped using graphite-monochromated Mo Kα radiation (0.71073 Å) source and operating in transmission mode. Fourier transform infrared (FTIR) spectra were recorded with PerkinElmer FTIR spectrophotometer 400 in the range 400–4000 cm^{-1}. Scanning electron micrographs were performed on a Nova Nano SEM 430 Company FEI (max. acceleration voltage 30 kV). Electron-X-ray spectroscopy was performed on an Apollo X EDAX (working distance 5 mm; entry angle 35°). The morphologies and composition of the samples were observed by Transmission Electron Microscope (TEM) using Zeiss LEO 912 instrument equipped with LaB_6-cathode operated at 120 kV high voltage. The dynamic light scattering experiments (DLS) were measured with a Malvern instruments Zetasizer Nano SZ. Phases of thin films were determined Magnetic measurements were performed with a superconducting quantum interference device (SQUID) magnetometer (Quantum Design, MPMS XL-7). Thermogravimetric analysis (TGA) characterization was performed on Netzsch STA 449C Jupiter. Samples were characterized in Al_2O_3 chamber in atmosphere of dry nitrogen or synthetic air (80% N_2 + 20% O_2), flow: 70 cm^3 min^{-1}, heating ramp 10 °C min^{-1} to 900 °C.

Conflicts of interest

The authors declare no competing financial conflict of interest.

Acknowledgements

We thank the University of Cologne and the "Deutscher Akademischer Austauschdienst" (DAAD) for their financial support. We also thank Dr Roitsch for TEM analysis, Mr Arroub for performing toxicity assays, Mr V. Vykoukal (Masaryk University, Brno, Czech Republic) for TGA measurements and Ms. N. Karamat for her help during particles synthesis. The authors thank Dr Wennhold and Prof. Schlößer for providing facilities to conduct cell tests with MCF 7 cells for flow cytometry measurements.

References

1 J. Shi, P. W. Kantoff, R. Wooster and O. C. Farokhzad, *Nat. Rev. Cancer*, 2017, **17**, 20–37.
2 D. Li, S. Wen, W. Sun, J. Zhang, D. Jin, C. Peng, M. Shen and X. Shi, *ACS Appl. Bio Mater.*, 2018, **1**, 221–225.
3 K. Ulbrich, K. Holá, V. Šubr, A. Bakandritsos, J. Tuček and R. Zbořil, *Chem. Rev.*, 2016, **116**, 5338–5431.
4 J. L. Bridot, A. C. Faure, S. Laurent, C. Rivière, C. Billotey, B. Hiba, M. Janier, V. Josserand, J. L. Coll, L. vander Elst, R. Muller, S. Roux, P. Perriat and O. Tillement, *J. Am. Chem. Soc.*, 2007, **129**, 5076–5084.
5 X. H. Ma, A. Gong, L. C. Xiang, T. X. Chen, Y. X. Gao, X. J. Liang, Z. Y. Shen and A. G. Wu, *J. Mater. Chem. B*, 2013, **1**, 3419–3428.
6 S. J. Kim, W. Xu, M. W. Ahmad, J. S. Baeck, Y. Chang, J. E. Bae, K. S. Chae, T. J. Kim, J. A. Park and G. H. Lee, *Sci. Technol. Adv. Mater.*, 2015, **16**, 1–9.
7 J. Y. Park, M. J. Baek, E. S. Choi, S. Woo, J. H. Kim, T. J. Kim, J. C. Jung, K. S. Chae, Y. Chang and G. H. Lee, *ACS Nano*, 2009, **3**, 3663–3669.
8 L. Faucher, M. Tremblay, J. Lagueux, Y. Gossuin and M. A. Fortin, *ACS Appl. Mater. Interfaces*, 2012, **4**, 4506–4515.
9 L. Zhou, Z. Gu, X. Liu, W. Yin, G. Tian, L. Yan, S. Jin, W. Ren, G. Xing, W. Li, X. Chang, Z. Hu and Y. Zhao, *J. Mater. Chem.*, 2012, **22**, 966–974.
10 B. Zhang, H. Jin, Y. Li, B. Chen, S. Liu and D. Shi, *J. Mater. Chem.*, 2012, **22**, 14494–14501.
11 W. Xu, J. Y. Park, K. Kattel, B. A. Bony, W. C. Heo, S. Jin, J. W. Park, Y. Chang, J. Y. Do, K. S. Chae, T. J. Kim, J. A. Park, Y. W. Kwak and G. H. Lee, *New J. Chem.*, 2012, **36**, 2361–2367.
12 S. Liu, H. Yue, S. L. Ho, S. Kim, J. A. Park, T. Tegafaw, M. Y. Ahmad, S. Kim, A. K. A. al Saidi, D. Zhao, Y. Liu, S. W. Nam, K. S. Chae, Y. Chang and G. H. Lee, *Int. J. Mol. Sci.*, 2022, **3**, 1792.

13 Z. Huang, Y. Wang, M. Wu, W. Li, H. Zuo, B. Xiao, X. Zhang, J. Wu, H. He and Q. Xia, *Mater. Des.*, 2021, **203**, 109600.
14 Z. Li, J. Guo, M. Zhang, G. Li and L. Hao, *Front. Chem.*, 2022, **10**, 1–10.
15 J. Wang, M. Zha, H. Zhao, W. Yue, D. Wu and K. Li, *Anal. Chem.*, 2022, **94**, 4005–4011.
16 J. Yin, X. Wang, H. Zheng, J. Zhang, H. Qu, L. Tian, F. Zhao and Y. Shao, *ACS Appl. Nano Mater.*, 2021, **4**, 3767–3779.
17 K. Cheng, M. Yang, R. Zhang, C. Qin, X. Su and Z. Cheng, *ACS Nano*, 2014, **8**, 9884–9896.
18 J. Yin, D. Chen, Y. Zhang, C. Li, L. Liu and Y. Shao, *Phys. Chem. Chem. Phys.*, 2018, **20**, 10038–10047.
19 K. Wang, L. An, Q. Tian, J. Lin and S. Yang, *RSC Adv.*, 2018, **8**, 26764–26770.
20 Y. Si, G. Zhang, D. Wang, C. Zhang, C. Yang, G. Bai, J. Qian, Q. Chen, Z. Zhang, Z. Wu, Y. Xu and D. Zou, *Chem. Eng. J.*, 2019, **360**, 289–298.
21 R. A. Sperling and W. J. Parak, *Philos. Trans. R. Soc., A*, 2010, **368**, 1333–1383.
22 R. Mout, D. F. Moyano, S. Rana and V. M. Rotello, *Chem. Soc. Rev.*, 2012, **41**, 2539–2544.
23 B. Pelaz, P. del Pino, P. Maffre, R. Hartmann, M. Gallego, S. Rivera-Fernández, J. M. de La Fuente, G. U. Nienhaus and W. J. Parak, *ACS Nano*, 2015, **9**, 6996–7008.
24 S. Ilyas, N. K. Ullah, M. Ilyas, K. Wennhold, M. Iqbal, H. A. Schlößer, M. S. Hussain and S. Mathur, *ACS Biomater. Sci. Eng.*, 2020, **6**, 6138–6147.
25 T. Perrier, P. Saulnier and J. P. Benoît, *Chem.–Eur. J.*, 2010, **16**, 11516–11529.
26 M. Renner, S. Ilyas, H. A. Schlößer, A. Szymura, S. Roitsch, K. Wennhold and S. Mathur, *Langmuir*, 2020, **36**, 14819–14828.
27 S. E. Bulun, D. Chen, M. Lu, H. Zhao, Y. Cheng, M. Demura, B. Yilmaz, R. Martin, H. Utsunomiya, S. Thung, E. Su, E. Marsh, A. Hakim, P. Yin, H. Ishikawa, S. Amin, G. Imir, B. Gurates, E. Attar, S. Reierstad, J. Innes and Z. Lin, *J. Steroid Biochem. Mol. Biol.*, 2007, **106**, 81–96.
28 M. B. Schütz, S. Ilyas, K. Lê, M. Valldor and S. Mathur, *ACS Appl. Nano Mater.*, 2020, **3**, 5936–5943.
29 L. Xiao, M. Mertens, L. Wortmann, S. Kremer, M. Valldor, T. Lammers, F. Kiessling and S. Mathur, *ACS Appl. Mater. Interfaces*, 2015, **7**, 6530–6540.
30 S. Aime, S. G. Crich, E. Gianolio, G. B. Giovenzana, L. Tei and E. Terreno, *Coord. Chem. Rev.*, 2006, **250**, 1562–1579.
31 J. S. Choi, J. H. Lee, T. H. Shin, H. T. Song, E. Y. Kim and J. Cheon, *J. Am. Chem. Soc.*, 2010, **132**, 11015–11017.
32 R. Ghosh Chaudhuri and S. Paria, *Chem. Rev.*, 2012, **112**, 2373–2433.
33 L. Wortmann, S. Ilyas, D. Niznansky, M. Valldor, K. Arroub, N. Berger, K. Rahme, J. Holmes and S. Mathur, *ACS Appl. Mater. Interfaces*, 2014, **6**, 16631–16642.
34 K. Yang, H. Peng, Y. Wen and N. Li, *Appl. Surf. Sci.*, 2010, **256**, 3093–3097.
35 N. Bogdan, F. Vetrone, G. A. Ozin and J. A. Capobianco, *Nano Lett.*, 2011, **11**, 835–840.
36 E. Hemmer, M. Quintanilla, F. Légaré and F. Vetrone, *Chem. Mater.*, 2015, **27**, 235–244.
37 B. Aiken, W. P. Hsu and E. Matijevik, Preparation and Properties of Monodispersed Colloidal Particles of Lanthanide Compounds: 111, Yttrium(III) and Mixed Yttrium(III)/Cerium(III) Systems, 1988.
38 Y. Wang, X. Peng, J. Shi, X. Tang, J. Jiang and W. Liu, *Nanoscale Res. Lett.*, 2012, **1**, 1–13.
39 G. Jian, Y. Liu, X. He, L. Chen and Y. Zhang, *Nanoscale*, 2012, **4**, 6336–6342.
40 G. Tian, Z. Gu, X. Liu, L. Zhou, W. Yin, L. Yan, S. Jin, W. Ren, G. Xing, S. Li and Y. Zhao, *J. Phys. Chem. C*, 2011, **115**, 23790–23796.
41 Y. Zheng, Y. Cheng, Y. Wang, F. Bao, L. Zhou, X. Wei, Y. Zhang and Q. Zheng, *J. Phys. Chem. B*, 2006, **110**, 3093–3097.
42 P. B. Shete, R. M. Patil, B. M. Tiwale and S. H. Pawar, *J. Magn. Magn. Mater.*, 2015, **377**, 406–410.
43 P. Araichimani, K. M. Prabu, G. Suresh Kumar, G. Karunakaran, N. van Minh, S. Karthi, E. K. Girija and E. Kolesnikov, *Ceram. Int.*, 2020, **46**, 18366–18372.
44 M. Mahdavi, M. bin Ahmad, M. J. Haron, F. Namvar, B. Nadi, M. Z. Ab Rahman and J. Amin, *Molecules*, 2013, **18**, 7533–7548.
45 (*a*) M. F. Attia, N. Anton, R. Bouchaala, P. Didier, Y. Arntz, N. Messaddeq, A. S. Klymchenko, Y. Mély and T. F. Vandamme, *RSC Adv.*, 2015, **5**, 74353–74361; (*b*) L. Lanlan, J. Guo and J. Wei, *J. Appl. Polym. Sci.*, 2014, **131**, 41058.
46 R. Mout, D. F. Moyano, S. Rana and V. M. Rotello, *Chem. Soc. Rev.*, 2012, **41**, 2539–2544.
47 A. Guay-Bégin, P. Chevallier, L. Faucher, S. Turgeon and M. A. Fortin, *Langmuir*, 2012, **28**, 774–782.
48 S. Ilyas, M. Ilyas, R. A. L. van der Hoorn and S. Mathur, *ACS Nano*, 2013, **7**, 9655–9663.
49 S. N. A. Jenie, S. Pace, B. Sciacca, R. D. Brooks, S. E. Plush and N. H. Voelcker, *ACS Appl. Mater. Interfaces*, 2014, **6**, 12012–12021.
50 C. Haensch, S. Hoeppener and U. S. Schubert, *Nanotechnology*, 2007, **19**, 035703.
51 M. Meldal and C. W. Tomøe, *Chem. Rev.*, 2008, **108**, 2952–3015.
52 H. Li, Q. Zheng and C. Han, *Analyst*, 2010, **135**, 1360–1364.
53 M. W. Brechbiel, *Q. J. Nucl. Med. Mol. Imaging*, 2008, **52**(2), 166.
54 M. Meisenheimer, S. Kürpig, M. Essler and E. Eppard, *Molecules*, 2008, **2**, 166.
55 L. M. Bronstein, X. Huang, J. Retrum, A. Schmucker, M. Pink, B. D. Stein and B. Dragnea, *Chem. Mater.*, 2007, **19**, 3624–3632.
56 E. Krakor, I. Gessner, M. Wilhelm, V. Brune, J. Hohnsen, L. Frenzen and S. Mathur, *MRS Commun.*, 2021, **11**, 363–371.
57 S. Ilyas, *Click Functionalized Nanoprobes for Target Specific Biomedical Applications*, Dr Hut Verlag, Universität Köln, 2015.
58 Z. A. Barra, N. M. Ferreira, M. A. Martins, H. Oliveira, L. P. Ferreira, M. M. Cruz, M. D. D. Carvalho, S. M. Neumayer, B. J. Rodriguez, C. Nunes and P. Ferreira, *J. Mater. Chem. B*, 2020, **8**, 1256–1265.
59 T. Ishiguchi and S. Takahashi, *Drugs R&D*, 2010, **10**, 133–145.